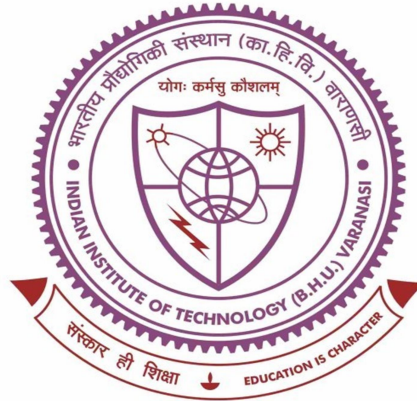


**ULTIMATE BEARING CAPACITY OF AXISYMMETRIC
AND PLANE-STRAIN FOUNDATIONS RESTED OVER
SATURATED/UNSATURATED STRATUM USING LIMIT
ANALYSIS**



A Thesis

Submitted for the Degree of
Doctor of Philosophy
In the Faculty of Engineering

By

SURYA DEV PRASAD

**Under the supervision of
Dr. Manash Chakraborty**

**DEPARTMENT OF CIVIL ENGINEERING
INDIAN INSTITUTE OF TECHNOLOGY
BANARAS HINDU UNIVERSITY
VARANASI-221005
INDIA**

17061010

2023

DECLARATIONS BY THE CANDIDATE

I, **SURYA DEV PRASAD**, certify that the work embodied in this thesis is my own bonafide work and carried out by me under the supervision of **Dr. Manash Chakraborty** from **July 2017 to July 2023** at the **Department of Civil Engineering, IIT(BHU), Varanasi**. The matter embodied in this has not been submitted for the award of any other/diploma. I declared that I have faithfully acknowledged and given credits to the research workers wherever their works have been cited in my work in this thesis. I further declare that I have not willfully copied any other's work, paragraphs, text, data, results, etc, reported in journals, book, magazines, reports dissertations, thesis, etc., or available at websites and included them in this thesis and cited as my own work.

Date: 10/7/2023

Place: Varanasi


(Surya Dev Prasad)

CERTIFICATE BY THE SUPERVISOR

It is certified that the above statement made by the student is correct to the best of my knowledge.



Dr. Manash Chakraborty

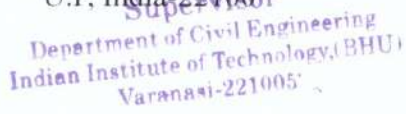
Supervisor

Asst. Professor

Dept. of Civil Engineering

IIT(BHU) Varanasi,

U.P, India-221005


Department of Civil Engineering
Indian Institute of Technology, (BHU)
Varanasi-221005

CERTIFICATE

It is certified that the work contained in the thesis titled "**ULTIMATE BEARING CAPACITY OF AXISYMMETRIC AND PLANE-STRAIN FOUNDATIONS RESTED OVER SATURATED/UNSATURATED STRATUM USING LIMIT ANALYSIS**" has been carried out under my supervision and this work has not been submitted elsewhere for a degree.

It is further certified that the student has fulfilled all the requirements of Comprehensive Examination, Candidacy, and State of the Art (SOTA) for the award of Ph.D degree.



Dr. Manash Chakraborty

Supervisor

Asst. Professor

Dept. of Civil engineering

IIT(BHU)

Varanasi, U.P, India-221005

COPYRIGHT TRANSFER CERTIFICATE

Title of the Thesis: **ULTIMATE BEARING CAPACITY OF AXISYMMETRIC AND PLANE-STRAIN FOUNDATIONS RESTED OVER SATURATED/UNSATURATED STRATUM USING LIMIT ANALYSIS**

Name of the Student: **Mr. Surya Dev Prasad**

Copyright Transfer

The undersigned hereby assigns to the Indian Institute of Technology, (BHU), Varanasi, all rights under copyright that may exist in and for the above thesis for the award of the Doctor of Philosophy.

Date: 10/7/23

Place: Varanasi


(Surya Dev Prasad)

Note: However, the author may reproduce or authorize others to reproduce material extracted verbatim from the thesis or derivative of the thesis for the author's personal use provided that the source and the Institute's copyright notice are indicated.

ACKNOWLEDGMENT

First and foremost, I would like to express my deepest gratitude to Lord Shiva for blessing me with countless opportunities, knowledge, and unwavering support, enabling me to complete this thesis successfully. Though my name appears on the cover, the accomplishment of this dissertation would not have been possible without the assistance and guidance of numerous individuals, to whom I owe my heartfelt appreciation.

I am immensely grateful to my supervisor, **Dr. Manash Chakraborty**, from the Civil Engineering Department at IIT (BHU), Varanasi, for his exceptional guidance, continuous monitoring, and unwavering encouragement throughout the entire duration of this research work. I am indebted to Dr. Manash Chakraborty for his invaluable inspiration and helpful recommendations, which significantly contributed to the completion of my research.

I extend my sincere appreciation to the members of my RPEC, Dr. Abhishek Mudggal as the internal expert and Dr. Joysurya Basu as the external expert, for their valuable assistance, insightful suggestions, and constant encouragement during the entirety of my research work.

Furthermore, I would like to express my gratitude to Prof. Sasankasekhar Mandal, Head of the Department of Civil Engineering, Indian Institute of Technology (BHU), Varanasi, for providing the necessary facilities for my research. My heartfelt regards go to Prof. Arun Prasad, Dr. Bala Ramudu Paramkusam, Dr. Suresh Kumar, Dr. Supriya Mohanty, and all the faculty members of the Civil Engineering Department for their unconditional support throughout my academic journey.

Special gratitude is extended to Dr. Dharendra Pal of Precision Instruments for his innovative ideas and continuous guidance throughout the course of my work. I am also thankful to my friends and colleague, Dr. Nitesh Bonal, Mrs. Shivani Dhiriyan, Dr. Parul Rawat, Mr. Amit Kumar Ram, Mr. Saurav Sarkar, Mr. Abhay Kumar, Mr. Amit Singh, Mr. Ankit Tiwari, Dr. Hitesh Upreti. Dr. Shambhavi Mishra and Dr. Gaurav Tiwari for their thought-provoking discussions, unwavering support, cooperation, and assistance in various ways.

In particular, I would like to express my heartfelt appreciation to some senior Mr. Manish Kumar Mandal, Dr. Bablesh Kumar Jha, Dr. Rahul Singh, Dr. Sujeet Kumar, Dr. Abhishek Kumar, Dr. Satyajee Mondal, Mr. Nitesh Gupta for their constant encouragement, love, and moral support. I take immense pleasure in sharing the credit for my research work with all my teachers who have played a significant role at different stages of my academic career.

Lastly, I am eternally grateful to my entire family for their unwavering faith, patience, encouragement, blessings, and unconditional love. My deepest appreciation goes to my father, Mr. Raja Ram Prasad, and my late mother, Late Humeli Prasad, for their unwavering motivation, belief in me, and continuous support. A special thanks to my special family for always holding my hand through the ups and downs, providing unwavering support and love.

I am sincerely grateful to each and every individual mentioned above, as well as those who have supported me in various ways, for their invaluable contributions to the completion of this thesis.

Surya Dev Prasad

CONTENTS

ACKNOWLEDGEMENT	iii
ABSTRACT	v
CONTENTS	xi
LIST OF FIGURES	xix
LIST OF TABLES	xxxiii
LIST OF NOTATIONS	xxxv
Chapter 1 INTRODUCTION	1
1.1 GENERAL	1
1.2 LIMIT ANALYSIS	3
1.3 BASIC TENENTS OF UNSATURATED SOIL MECHANICS (USM)	5
1.3.1 Soil-Water Retention Curve	7
1.3.1.1 van-Genuchten SWRC model (1980)	11
1.3.2 Gardner’s Hydraulic Conductivity Function (1958)	12
1.3.3 Flow Law	12
1.3.4 Effective stress	13
1.3.5 Introduction of Suction stress	14
1.4 BRIEF OUTLINE OF THESIS	16
1.5 ORGANIZATION OF THE THESIS	17
Chapter 2 LITERATURE REVIEW	19
2.1 INTRODUCTION	19
2.2 LITERATURE REVIEW: LIMIT ANALYSIS	19
2.2.1 Hayes and Marcal (1967)	20
2.2.2 Lysmer (1970)	20
2.2.3 Anderheggen and Knopfel (1972)	21
2.2.4 Basudhar et al. (1979)	21
2.2.5 Bottero et al. (1980)	22
2.2.6 Pastor and Turgeman (1982)	22
2.2.7 Arai and Tagyo (1985)	23

2.2.8 Sloan (1988)	23
2.2.9 Sloan (1989)	23
2.2.10 Sloan and Kleeman (1995)	24
2.2.11 Lyamin and Sloan (2002a)	24
2.2.12 Lyamin and Sloan (2002b)	25
2.2.13 Krabbenhoft and Damkilde (2003)	25
2.2.14 Krabbenhoft et al. (2005)	26
2.2.15 Makrodimopoulos and Martin (2006)	26
2.2.16 Makrodimopoulos and Martin (2007)	26
2.2.17 Krabbenhoft et al. (2007)	27
2.2.18 Kumar and Khatri (2011)	27
2.2.19 Kumar and Chakraborty (2013)	28
2.2.20 Chakraborty and Kumar (2014)	28
2.2.21 Chakraborty and Kumar (2015)	29
2.2.22 Mohapatra and Kumar (2018)	29
2.2.23 Ukritchon and Keawsawasvong (2018)	29
2.3 LITERATURE REVIEW: ULTIMATE BEARING CAPACITY OF RING FOOTING	30
2.3.1 Ismael (1995)	30
2.3.2 Boushehrian and Hataf (2003)	31
2.3.3 Hataf and Razavi (2003)	31
2.3.4 Kumar and Ghosh (2005)	32
2.3.5 Zhao and Wang (2008)	32
2.3.6 Benmebarek et al. (2012)	32
2.3.7 Moayed et al. (2012)	33
2.3.8 Sawwaf and Nazir (2012)	33
2.3.9 Demir et al. (2014)	34
2.3.10 Naseri and Hosseininia (2015)	34
2.3.11 Kumar and Chakraborty (2015)	35
2.3.12 Keshavarz and Kumar (2017)	35
2.3.13 Benmebarek et al. (2017)	36
2.3.14 Gholami and Hosseininia (2017)	36

Contents	xiii
2.3.15 Tang and Phoon (2018)	37
2.3.16 Chavda and Dodagaudar (2019)	38
2.3.17 Turedi et al. (2019)	38
2.3.18 Vali et al. (2019)	39
2.3.19 Das et al. (2019)	39
2.3.20 Chavda and Dodagoudar (2021)	40
2.3.21 Hussein (2021)	40
2.4 LITERATURE REVIEW: ULTIMATE BEARING CAPACITY OF STRIP FOOTINGS ON UNSATURATED SOILS MECHANICS (USM)	41
2.4.1 Vanapalli and Mohamed (2007)	42
2.4.2 Oh and Vanapalli (2008)	42
2.4.3 Oh and Vanapalli (2013)	42
2.4.4 Vanapalli and Mohamed (2013)	43
2.4.5 Vo and Russell (2016)	44
2.4.6 Vahedifard and Robinson (2016)	44
2.4.7 Oh and Vanapalli (2017)	44
2.4.8 Tang et al. (2017)	45
2.4.9 Ghasemzadeh and Akbari (2019)	45
2.4.10 Garakani et al. (2019)	46
2.4.11 Anand and Sarkar (2020)	46
2.4.12 Du et al. (2020)	47
2.4.13 Yan et al. (2020)	47
2.4.14 Afsharpour et al. (2022)	48
2.4.15 Anand and Sarkar (2022)	48
2.4.16 Fathipour et al. (2022)	49
2.4.17 Tan and Vanapalli (2023)	49
2.4.18 Yilmazoglu and Ozocak (2023)	50
2.4.19 Roy and Chakraborty (2023)	50
2.5 RESEARCH GAP AND OBJECTIVES OF THE PRESENT THESIS	50
2.6 SUMMARY	53

Chapter 3 COMPUTATIONAL PROCEDURE FOR LOWER BOUND	
FELA WITH NONLINEAR OPTIMIZATIO	55
3.1 INTRODUCTION	55
3.2 LOWER BOUND LIMIT ANALYSIS FORMULATION	57
3.2.1 Discretization of domain	57
3.2.2 Element equilibrium condition	57
3.2.3 Statically admissible stress discontinuity condition	59
3.2.4 Stress boundary condition	61
3.2.5 Soil-footing interface condition for a footing problem	62
3.2.6 Yield functions	62
3.2.6.1 Mohr-Coulomb yield function	64
3.2.6.2 Tresca yield function	64
3.2.7 Objective function	66
3.2.8 Form of the Optimization Problem	67
3.2.9 Smoothing the yield surfaces	68
3.2.9.1 Smoothing in the meridian plane (for MC surface)	69
3.2.9.2 Smoothing in the deviatoric plane (for MC and Tresca surfaces)	70
3.2.10 Procedure	74
3.3 NUMERICAL EXAMPLE- ULTIMATE BEARING CAPACITY FACTORS FOR PILE FOOTING EMBEDDED INTO A NON-HOMOGENOUS CLAYEY SOIL	77
3.3.1 Problem definition	77
3.3.2 Problem domain, boundary conditions and mesh details	77
3.3.3 Results and Discussion	80
3.3.3.1 Numerical solutions	80
3.3.3.2 Failure patterns	81
3.3.4 Comparisons with the available solutions	84
3.4 SUMMARY	86
Chapter 4 ULTIMATE BEARING CAPACITY OF RING FOOTING RESTED ON TWO-LAYERED SOILS	89
4.1 INTRODUCTION	89

Chapter 6	ULTIMATE BEARING CAPACITY FACTORS FOR RING FOOTING ON ROCKMASS DUE TO VARIOUS LOADING POSITIONS	193
6.1	INTRODUCTION	193
6.2	PROBLEM STATEMENT AND DOMAIN	195
6.3	HOEK-BROWN YIELD CRITERION	197
6.4	ANALYSIS	201
6.5	SMOOTHENING OF THE GHB CRITERION	201
6.6	RESULTS AND DISCUSSION	205
6.6.1	Chosen parameters and UBC	205
6.6.2	Impact of ring geometry and surcharging	206
6.6.3	Impact of rock strength	210
6.6.4	Failure patterns	213
6.7	COMPARISONS OF RESULTS	218
6.8	SUMMARY	221
Chapter 7	ULTIMATE BEARING CAPACITY OF STRIP FOUNDATION ON UNSATURATED SOIL BY UB-FELA TECHNIQUE	223
7.1	INTRODUCTION	223
7.2	CONSTRUCTION OF SSCC CURVES	225
7.3	IMPACT OF THE MODEL PARAMETERS ON SWRC, HCF, AND SSCC MODELS	226
7.3.1	van -Genuchten's SWRC model	226
7.3.2	Gardner's HCF model	228
7.3.3	Lu and Likos's SSCC model	229
7.4	UPPER BOUND FINITE ELEMENT LIMIT ANALYSIS FORMULATION	229
7.4.1	Constraints within the elements arising from the plastic flow	232
7.4.2	Constraints arising from plastic flow along velocity discontinuities	234
7.4.3	Constraints arising due to velocity boundary conditions	236
7.4.4	Objective function	237
7.4.4.1	The rate of work done by the body forces	238
7.4.4.2	Power dissipation in continuum due to plastic deformation	238

Contents	xvii
<hr/>	
7.4.4.3 Power dissipation along the velocity discontinuities	239
7.4.4.4 Assembling the constraint equations and objective function	240
7.4.5 Solution procedure for linear optimization	241
7.5 NUMERICAL EXAMPLE:- BEARING CAPACITY OF STRIP FOOTING ON UNSATURATED SANDY SOIL	242
7.5.1 Problem statement and Domain	242
7.5.2 Results and Discussion	245
7.5.3 Nodal velocity patterns	252
7.5.4 Comparisons of results	257
7.6 LIMITATIONS	260
7.7 SUMMARY	260
Chapter 8 ULTIMATE BEARING CAPACITY OF STRIP FOOTING ON UNSATURATED SANDY SOIL UNDER COMBINED LOAD	263
8.1 INTRODUCTION	263
8.2 PROBLEM STATEMENT AND DOMAIN	264
8.3 ANALYSIS	266
8.4 RESULTS AND DISCUSSION	269
8.4.1 Bearing capacity charts	269
8.4.2 Normalized V-H failure envelopes	280
8.4.3 Nodal Velocity Patterns	282
8.5 COMPARISONS OF RESULTS	289
8.6 SUMMARY	291
Chapter 9 ULTIMATE BEARING CAPACITY OF STRIP FOOTING ON UNSATURATED SANDY SOIL DUE TO TRANSIENT FLOW	293
9.1 INTRODUCTIO	293
9.2 PROBLEM STATEMENT AND DOMAIN	294
9.3 SUCTION STRESS AND ANALYSIS PROCEDURE	295
9.3.1 Evaluating suction stress due to transient flow	295
9.3.2 Variation of the Suction Stress Profiles	298
9.3.3 Analysis	301

9.4 RESULTS AND DISCUSSION	302
9.4.1 Transient ultimate Bearing Capacity	302
9.4.2 Nodal Velocity Pattern	308
9.5 SUMMARY	312
Chapter 10 SUMMARY, CONCLUSIONS, AND FUTURE SCOPE	313
10.1 SUMMARY	313
10.2 CONCLUSIONS	315
10.3 LIMITATIONS AND FUTURE SCOPE	322
REFERENCES	325
Appendix-A: ALGORITHM FOR SOLVING NON-LINEAR OPTIMIZATION PROBLEM	353
Appendix-B: GRADIENT AND HESSIAN OF SMOOTHENED MOHR- COULOMB YIELD FUNCTION	355
Appendix-C: GRADIENT AND HESSIAN OF SMOOTHENED TRESCA YIELD FUNCTION	359
Appendix-D: GRADIENT AND HESSIAN OF SMOOTHENED HOEK- BROWN YIELD FUNCTION	361
Appendix-E: CRANK-NICOLSON FINITE DIFFERENCE IMPLICIT TECHNIQUE	367
LIST OF PUBLICATIONS	369

LIST OF FIGURES

Figure No.	Title	Page No.
Figure 1.1	The variation of matric suction profiles in the unsaturated zone.	6
Figure 1.2	Typical features of the soil–water retention curve (SWRC) (modified after Vanapalli et al. (1996).	8
Figure 1.3	The matric suction profile in three-dimensional: a) $\tau-\psi$ – $(\sigma-u_a)$; and b) $\tau-\sigma^s$ – $(\sigma-u_a)$ spaces.	15
Figure 3.1	a) Pictorial representation of element equilibrium within an element; and b) the sign convention for normal and shear stresses.	58
Figure 3.2	a) Stress discontinuity condition along the interface shared by two adjacent elements, a and b ; and b) stress boundary conditions along any edge 1-2.	59
Figure 3.3	a) Original form of Mohr-Coulomb surface in 3-D principal space; (b-c) 2-D planes (meridian and deviatoric).	65
Figure 3.4.	a) Tresca yield surface in 3D principal space; and b) Tresca surface in octrahedral plane.	66
Figure 3.5	Normal stresses acting along any boundary surface, s .	67
Figure 3.6	Smooth hyperbolic approximation of MC yield surface in meridian section.	70
Figure 3.7	Mohr-Coulomb yield surface in a π -plane a) with sharp vertices; b) rounded hyperbolic form (C^2 -continuity) of one side of the hexagon; and c) complete rounded surface for $\phi = 0$ (Tresca) case.	73
Figure 3.8.	a) Problem domain and associated boundary conditions; b) variation of cohesion within the soil domain.	78
Figure 3.9	Finite Element meshes for $\alpha_b = 1$, $\alpha_s = 1$	78
Figure 3.10	The variation of N_c with respect to m for different H/B ratio of pile for $\alpha_b = 1$, $\alpha_s = 1$.	80
Figure 3.11	The variation of N_c with respect to m for different roughness conditions at the pile base and pile shaft.	81
Figure 3.12	Schematic diagram of Mohr's stress circle at failure and current stress state for any arbitrary point in the domain.	82

Figure 3.13	Failure pattern for $H/B= 1$ with $\alpha_b= 1$, $\alpha_s = 0$ and a) $m= 0$; and b) $m= 4$.	83
Figure 3.14	Failure patterns for $m= 0$ with: a) $H/B= 0.5$, $\alpha_b= 1$, $\alpha_s = 0$; b) $H/B= 2$, $\alpha_b = 1$, $\alpha_s = 0$; and c) $H/B= 2$, $\alpha_b = 1$, $\alpha_s = 1$.	83
Figure 3.15	A comparison of the variation of N_c with H/B for homogeneous clays ($m = 0$).	84
Figure 4.1	Chosen domain and the stress boundary conditions for ring footing on sandy-clay layered medium and cohesion increment in the bottom layer.	93
Figure 4.2	Finite Element Mesh for for $\phi = 35^\circ$ and $c_u/\gamma r_0 = 0.5$ with: a) $h/r_0=1$, $r_i/r_0=0$; b) $h/r_0=2$, $r_i/r_0=0.25$.	94
Figure 4.3	The variation of η with respect to h/r_0 for different smooth and rough annular footing resting on sands having $\phi = 30^\circ$ and underlain by various homogenous cohesive stratum with varying surcharge: (a-d) $q/(\gamma r_0)=0.0$; (e-h) $q/(\gamma r_0)=0.5$; (i-l) $q/(\gamma r_0)=1.0$.	98
Figure 4.4	The variation of η with respect to h/r_0 for different smooth and rough annular footing resting on sands having $\phi = 35^\circ$ and underlain by various homogenous cohesive stratum with varying surcharge: (a-d) $q/(\gamma r_0)=0.0$; (e-h) $q/(\gamma r_0)=0.5$; (i-l) $q/(\gamma r_0)=1.0$.	99
Figure 4.5	The variation of η with respect to h/r_0 for different smooth and rough annular footing resting on sands having $\phi = 40^\circ$ and underlain by various homogenous cohesive stratum with varying surcharge: (a-d) $q/(\gamma r_0)=0.0$; (e-h) $q/(\gamma r_0)=0.5$; (i-l) $q/(\gamma r_0)=1.0$.	100
Figure 4.6	The variation of η with respect to h/r_0 for different smooth and rough annular footing resting on sands having $\phi = 45^\circ$ and underlain by various homogenous cohesive stratum with varying surcharge: (a-d) $q/(\gamma r_0)=0.0$; (e-h) $q/(\gamma r_0)=0.5$; (i-l) $q/(\gamma r_0)=1.0$.	101
Figure 4.7	The variation of η with respect to h/r_0 for different annular footing corresponding to two different sands, $\phi = 30^\circ$ and 35° , overlying on various cohesive layer having $m = 2$ and subjected to varying surcharge: (a-d) $q/(\gamma r_0)=0.0$; (e-h) $q/(\gamma r_0)=0.5$; (i-l) $q/(\gamma r_0)=1.0$.	102
Figure 4.8	The variation of η with respect to h/r_0 for different annular footing corresponding to two different sands, $\phi = 40^\circ$ and 45° , overlying on various cohesive layer having $m = 2$ and subjected to varying surcharge: (a-d) $q/(\gamma r_0)=0.0$; (e-h) $q/(\gamma r_0)=0.5$; (i-l) $q/(\gamma r_0)=1.0$.	103

- Figure 4.9** The variation of η with respect to h/r_0 for different annular footing corresponding to two different sands, $\phi = 30^\circ$ and 35° , overlying on various cohesive layer, having $m = 5$, and subjected to varying surcharge: (a-d) $q/(\gamma r_0) = 0.0$; (e-h) $q/(\gamma r_0) = 0.5$; (i-l) $q/(\gamma r_0) = 1.0$. 204
- Figure 4.10** The variation of η with respect to h/r_0 for different annular footing corresponding to two different sands, $\phi = 40^\circ$ and 45° , overlying on various cohesive layer, having $m = 5$, and subjected to varying surcharge: (a-d) $q/(\gamma r_0) = 0.0$; (e-h) $q/(\gamma r_0) = 0.5$; (i-l) $q/(\gamma r_0) = 1.0$. 105
- Figure 4.11** The variation of η with respect to footing roughness corresponding to three different $c_u/(\gamma r_0)$, namely, 0.1, 1.0, and 10 with optimum sand thickness and for following different cases: a) $\phi = 30^\circ$, $m = 0$; b) $\phi = 30^\circ$, $m = 2$; c) $\phi = 30^\circ$, $m = 5$; d) $\phi = 40^\circ$, $m = 0$; e) $\phi = 40^\circ$, $m = 2$; and f) $\phi = 40^\circ$, $m = 5$. 111
- Figure 4.12** Failure pattern for $c_u/(\gamma r_0) = 1$, $q/(\gamma r_0) = 0$, $h/r_0 = 2$, and $r_i/r_0 = 0.25$ with various value of ϕ : a) $\phi = 30^\circ$; b) $\phi = 35^\circ$; c) $\phi = 40^\circ$; and d) $\phi = 45^\circ$. 114
- Figure 4.13** Failure pattern $\phi = 35^\circ$, $q/(\gamma r_0) = 0$, $h/r_0 = 1$, and $r_i/r_0 = 0.25$ with: a) $c_u/(\gamma r_0) = 0.1$; b) $c_u/(\gamma r_0) = 1$; c) $c_u/(\gamma r_0) = 5$; and d) $c_u/(\gamma r_0) = 10$. 115
- Figure 4.14** Failure pattern for $\phi = 35^\circ$, $q/(\gamma r_0) = 0$, $r_i/r_0 = 0.25$, and $c_u/(\gamma r_0) = 0.5$ corresponding to: a) $h/r_0 = 0.25$; b) $h/r_0 = 2$; c) $h/r_0 = 5$; and d) $h/r_0 = 10$. 116
- Figure 4.15** Failure pattern for $\phi = 35^\circ$, $q/(\gamma r_0) = 0.5$, $h/r_0 = 2$, and $c_u/(\gamma r_0) = 1$ with: a) $r_i/r_0 = 0$; b) $r_i/r_0 = 0.25$; c) $r_i/r_0 = 0.5$; and d) $r_i/r_0 = 0.75$. 117
- Figure 4.16** Failure pattern for $\phi = 40^\circ$, $r_i/r_0 = 0.25$, $h/r_0 = 6$, $q/(\gamma r_0) = 1$, and $c_u/(\gamma r_0) = 10$ with: a) $\delta/\phi = 0$; b) $\delta/\phi = 0.2$; c) $\delta/\phi = 0.4$; and d) $\delta/\phi = 0.6$. 118
- Figure 4.17** Failure pattern for $\phi = 40^\circ$, $r_i/r_0 = 0.25$, $h/r_0 = 2$, and $c_u/(\gamma r_0) = 0.1$ with: a) $q/(\gamma r_0) = 0$; b) $q/(\gamma r_0) = 0.5$; and c) $q/(\gamma r_0) = 1$. 119
- Figure 4.8** The variation of η with respect to h/r_0 for different annular footing corresponding to two different sands, $\phi = 40^\circ$ and 45° , overlying on various cohesive layer having $m = 2$ and subjected to varying surcharge: (a-d) $q/(\gamma r_0) = 0.0$; (e-h) $q/(\gamma r_0) = 0.5$; (i-l) $q/(\gamma r_0) = 1.0$. 103
- Figure 4.9** The variation of η with respect to h/r_0 for different annular footing corresponding to two different sands, $\phi = 30^\circ$ and 35° , overlying 204

on various cohesive layer, having $m = 5$, and subjected to varying surcharge: (a-d) $q/(\gamma r_0) = 0.0$; (e-h) $q/(\gamma r_0) = 0.5$; (i-l) $q/(\gamma r_0) = 1.0$.

- Figure 4.10** The variation of η with respect to h/r_0 for different annular footing corresponding to two different sands, $\phi = 40^\circ$ and 45° , overlying on various cohesive layer, having $m = 5$, and subjected to varying surcharge: (a-d) $q/(\gamma r_0) = 0.0$; (e-h) $q/(\gamma r_0) = 0.5$; (i-l) $q/(\gamma r_0) = 1.0$. 105
- Figure 4.11** The variation of η with respect to footing roughness corresponding to three different $c_u/(\gamma r_0)$, namely, 0.1, 1.0, and 10 with optimum sand thickness and for following different cases: a) $\phi = 30^\circ$, $m = 0$; b) $\phi = 30^\circ$, $m = 2$; c) $\phi = 30^\circ$, $m = 5$; d) $\phi = 40^\circ$, $m = 0$; e) $\phi = 40^\circ$, $m = 2$; and f) $\phi = 40^\circ$, $m = 5$. 111
- Figure 4.12** Failure pattern for $c_u/(\gamma r_0) = 1$, $q/(\gamma r_0) = 0$, $h/r_0 = 2$, and $r_i/r_0 = 0.25$ with various value of ϕ : a) $\phi = 30^\circ$; b) $\phi = 35^\circ$; c) $\phi = 40^\circ$; and d) $\phi = 45^\circ$. 114
- Figure 4.13** Failure pattern $\phi = 35^\circ$, $q/(\gamma r_0) = 0$, $h/r_0 = 1$, and $r_i/r_0 = 0.25$ with: a) $c_u/(\gamma r_0) = 0.1$; b) $c_u/(\gamma r_0) = 1$; c) $c_u/(\gamma r_0) = 5$; and d) $c_u/(\gamma r_0) = 10$. 115
- Figure 4.14** Failure pattern for $\phi = 35^\circ$, $q/(\gamma r_0) = 0$, $r_i/r_0 = 0.25$, and $c_u/(\gamma r_0) = 0.5$ corresponding to: a) $h/r_0 = 0.25$; b) $h/r_0 = 2$; c) $h/r_0 = 5$; and d) $h/r_0 = 10$. 116
- Figure 4.15** Failure pattern for $\phi = 35^\circ$, $q/(\gamma r_0) = 0.5$, $h/r_0 = 2$, and $c_u/(\gamma r_0) = 1$ with: a) $r_i/r_0 = 0$; b) $r_i/r_0 = 0.25$; c) $r_i/r_0 = 0.5$; and d) $r_i/r_0 = 0.75$. 117
- Figure 4.16** Failure pattern for $\phi = 40^\circ$, $r_i/r_0 = 0.25$, $h/r_0 = 6$, $q/(\gamma r_0) = 1$, and $c_u/(\gamma r_0) = 10$ with: a) $\delta/\phi = 0$; b) $\delta/\phi = 0.2$; c) $\delta/\phi = 0.4$; and d) $\delta/\phi = 0.6$. 118
- Figure 4.17** Failure pattern for $\phi = 40^\circ$, $r_i/r_0 = 0.25$, $h/r_0 = 2$, and $c_u/(\gamma r_0) = 0.1$ with: a) $q/(\gamma r_0) = 0$; b) $q/(\gamma r_0) = 0.5$; and c) $q/(\gamma r_0) = 1$. 119
- Figure 4.18** Failure pattern for $\phi = 35^\circ$, $r_i/r_0 = 0.25$, $h/r_0 = 2$, $q/(\gamma r_0) = 0.5$, and $c_u/(\gamma r_0) = 1$ with: a) $m = 0$; b) $m = 2$; and c) $m = 5$. 119
- Figure 5.1** Ring footing rested over two layered, as represented in a) three-dimensional axisymmetric form, b) two-dimensional form; and c) three different configurations of loadings. 132
- Figure 5.2** Mesh used for the ring footing corresponding to $\phi_1 = 30^\circ$, $\phi_2 = 35^\circ$, and for four different radius ratios: a) $r_i/r_0 = 0$; b) $r_i/r_0 = 0.25$; c) $r_i/r_0 = 0.50$; and d) $r_i/r_0 = 0.75$. 134

- Figure 5.3** The variations of normalized bearing capacity with respect to r_i/r_0 for smooth and rough ring footing resting on a sand layer having $\phi_1=30^\circ$ and different values of ϕ_2 with $q/(\gamma r_0)=0$ and corresponding to three different loading positions: (a–d) L_1 ; (e–h) L_2 ; and (i–l) L_3 . 138
- Figure 5.4** The variations of normalized bearing capacity with respect to r_i/r_0 for smooth and rough ring footing resting on a sand layer having $\phi_1=30^\circ$ and different values of ϕ_2 with $q/(\gamma r_0)=1$ and corresponding to three different loading positions: (a–d) L_1 ; (e–h) L_2 ; and (i–l) L_3 . SL: solid line; and DL: dashed line. 139
- Figure 5.5** The variations of normalized bearing capacity with respect to r_i/r_0 for smooth and rough ring footing resting on a sand layer having $\phi_1=35^\circ$ and different values of ϕ_2 with $q/(\gamma r_0)=0$ and corresponding to three different loading positions: (a–d) L_1 ; (e–h) L_2 ; and (i–l) L_3 . SL: solid line; and DL: dashed line. 140
- Figure 5.6** The variations of normalized bearing capacity with respect to r_i/r_0 for smooth and rough ring footing resting on a sand layer having $\phi_1=35^\circ$ and different values of ϕ_2 with $q/(\gamma r_0)=1$ and corresponding to three different loading positions: (a–d) L_1 ; (e–h) L_2 ; and (i–l) L_3 . SL: solid line; and DL: dashed line. 141
- Figure 5.7** The variations of normalized bearing capacity with respect to r_i/r_0 for smooth and rough ring footing resting on a sand layer having $\phi_1=40^\circ$ and different values of ϕ_2 with $q/(\gamma r_0)=0$ and corresponding to three different loading positions: (a–d) L_1 ; (e–h) L_2 ; and (i–l) L_3 . SL: solid line; and DL: dashed line. 142
- Figure 5.8** The variations of normalized bearing capacity with respect to r_i/r_0 for smooth and rough ring footing resting on a sand layer having $\phi_1=40^\circ$ and different values of ϕ_2 with $q/(\gamma r_0)=1$ and corresponding to three different loading positions: (a–d) L_1 ; (e–h) L_2 ; and (i–l) L_3 . SL: solid line; and DL: dashed line. 143
- Figure 5.9** The variations of normalized bearing capacity with respect to r_i/r_0 for smooth and rough ring footing resting on a sand layer having $\phi_1=45^\circ$ and different values of ϕ_2 with $q/(\gamma r_0)=0$ and corresponding to three different loading positions: (a–d) L_1 ; (e–h) L_2 ; and (i–l) L_3 . SL: solid line; and DL: dashed line. 144
- Figure 5.10** The variations of normalized bearing capacity with respect to r_i/r_0 145

for smooth and rough ring footing resting on a sand layer having $\phi_1=45^\circ$ and different values of ϕ_2 with $q/(\gamma r_0)=1$ and corresponding to three different loading positions: (a–d) L_1 ; (e–h) L_2 ; and (i–l) L_3 . SL: solid line; and DL: dashed line.

- Figure 5.11** The variation of η with respect to h/r_0 for ring footing resting on layered sands ($\phi_1=30^\circ$) corresponding to with and without surcharge and four different radius ratios: (a and e) $r_i/r_0=0$; (b and f) $r_i/r_0=0.25$; (c and g) $r_i/r_0=0.50$; and (d and h) $r_i/r_0=0.75$. 148
- Figure 5.12** The variation of η with respect to h/r_0 for ring footing resting on layered sands ($\phi_1=35^\circ$) corresponding to with and without surcharge and four different radius ratios: (a and e) $r_i/r_0=0$; (b and f) $r_i/r_0=0.25$; (c and g) $r_i/r_0=0.50$; and (d and h) $r_i/r_0=0.75$. 149
- Figure 5.13** The variation of η with respect to h/r_0 for ring footing resting on layered sands ($\phi_1=40^\circ$) corresponding to with and without surcharge and four different radius ratios: (a and e) $r_i/r_0=0$; (b and f) $r_i/r_0=0.25$; (c and g) $r_i/r_0=0.50$; and (d and h) $r_i/r_0=0.75$. 150
- Figure 5.14** The variation of η with respect to h/r_0 for ring footing resting on layered sands ($\phi_1 = 45^\circ$) corresponding to with and without surcharge and four different radius ratios: (a and e) $r_i/r_0=0$; (b and f) $r_i/r_0=0.25$; (c and g) $r_i/r_0=0.50$; and (d and h) $r_i/r_0=0.75$. 151
- Figure 5.15** The variation of UBC with respect to r_i/r_0 for ring footing resting on clayey soil having cohesion ($c_{u1}/(\gamma r_0)=0.25$) overlying on clayey soils ($c_{u2}/(\gamma r_0)$) and corresponding to three different loading positions: a) L_1 ; b) L_2 ; c) L_3 . 153
- Figure 5.16** The variation of UBC with respect to r_i/r_0 for ring footing resting on clayey soil having cohesion ($c_{u1}/(\gamma r_0)=0.50$) overlying on clayey soils ($c_{u2}/(\gamma r_0)$) and corresponding to three different loading positions: (a-d) L_1 ; (e-h) L_2 ; (i-l) L_3 . 154
- Figure 5.17** The variation of UBC with respect to r_i/r_0 for ring footing resting on clayey soil having cohesion ($c_{u1}/(\gamma r_0)=1.0$) overlying on clayey soils ($c_{u2}/(\gamma r_0)$) and corresponding to three different loading positions: (a-d) L_1 ; (e-h) L_2 ; (i-l) L_3 . 155
- Figure 5.18** The variation of UBC with respect to r_i/r_0 for ring footing resting on clayey soil having cohesion ($c_{u1}/(\gamma r_0)=2.0$) overlying on clayey soils ($c_{u2}/(\gamma r_0)$) and corresponding to three different loading positions: (a-d) L_1 ; (e-h) L_2 ; (i-l) L_3 . 156

- Figure 5.19** The variation of η with respect to h/r_0 for ring footing resting on layered clays corresponding to four different radius ratios: (a and e) $r_i/r_0=0$; (b and f) $r_i/r_0=0.25$; (c and g) $r_i/r_0=0.50$; and (d and h) $r_i/r_0=0.75$. 158
- Figure 5.20** The variation of η with respect to h/r_0 for ring footing resting on layered clays corresponding to four different radius ratios: (a and e) $r_i/r_0=0$; (b and f) $r_i/r_0=0.25$; (c and g) $r_i/r_0=0.50$; and (d and h) $r_i/r_0=0.75$. 159
- Figure 5.21** The variation of normalized bearing capacity with respect to r_i/r_0 for smooth and rough ring footing resting on a sand layer having $\phi = 30^\circ$ and different values of $c_u/(\gamma r_0)$ with $q/(\gamma r_0) = 0$ and corresponding to three different loading positions: (a-d) L_1 ; (e-h) L_2 ; and (i-l) L_3 . 161
- Figure 5.22** The variation of normalized bearing capacity with respect to r_i/r_0 for smooth and rough ring footing resting on a sand layer having $\phi = 30^\circ$ and different values of $c_u/(\gamma r_0)$ with $q/(\gamma r_0) = 1$ and corresponding to three different loading positions: (a-d) L_1 ; (e-h) L_2 ; and (i-l) L_3 . 162
- Figure 5.23** The variation of normalized bearing capacity with respect to r_i/r_0 for smooth and rough ring footing resting on a sand layer having $\phi = 35^\circ$ and different values of $c_u/(\gamma r_0)$ with $q/(\gamma r_0) = 0$ and corresponding to three different loading positions: (a-d) L_1 ; (e-h) L_2 ; and (i-l) L_3 . 163
- Figure 5.24** The variation of normalized bearing capacity with respect to r_i/r_0 for smooth and rough ring footing resting on a sand layer having $\phi = 35^\circ$ and different values of $c_u/(\gamma r_0)$ with $q/(\gamma r_0) = 1$ and corresponding to three different loading positions: (a-d) L_1 ; (e-h) L_2 ; and (i-l) L_3 . 164
- Figure 5.25** The variation of normalized bearing capacity with respect to r_i/r_0 for smooth and rough ring footing resting on a sand layer having $\phi = 40^\circ$ and different values of $c_u/(\gamma r_0)$ with $q/(\gamma r_0) = 0$ and corresponding to three different loading positions: (a-d) L_1 ; (e-h) L_2 ; and (i-l) L_3 . 165
- Figure 5.26** The variation of normalized bearing capacity with respect to r_i/r_0 for smooth and rough ring footing resting on a sand layer having $\phi = 40^\circ$ and different values of $c_u/(\gamma r_0)$ with $q/(\gamma r_0) = 1$ and 166

- corresponding to three different loading positions: (a-d) L_1 ; (e-h) L_2 ; and (i-l) L_3 .
- Figure 5.27** The variation of normalized bearing capacity with respect to r_i/r_0 for smooth and rough ring footing resting on a sand layer having $\phi = 45^\circ$ and different values of $c_u/(\gamma r_0)$ with $q/(\gamma r_0) = 0$ and corresponding to three different loading positions: (a-d) L_1 ; (e-h) L_2 ; and (i-l) L_3 . 167
- Figure 5.28** The variation of normalized bearing capacity with respect to r_i/r_0 for smooth and rough ring footing resting on a sand layer having $\phi = 45^\circ$ and different values of $c_u/(\gamma r_0)$ with $q/(\gamma r_0) = 1$ and corresponding to three different loading positions: (a-d) L_1 ; (e-h) L_2 ; and (i-l) L_3 . 168
- Figure 5.29** The variation of η with respect to h/r_0 for ring footing resting on sandy-clayey with ($\phi=30^\circ$) and corresponding to four different radius ratios: (a and e) $r_i/r_0=0$; (b and f) $r_i/r_0=0.25$; (c and g) $r_i/r_0=0.50$; and (d and h) $r_i/r_0=0.75$. 170
- Figure 5.30** The variation of η with respect to h/r_0 for ring footing resting on sandy-clayey with ($\phi=35^\circ$) and corresponding to four different radius ratios: (a and e) $r_i/r_0=0$; (b and f) $r_i/r_0=0.25$; (c and g) $r_i/r_0=0.50$; and (d and h) $r_i/r_0=0.75$. 171
- Figure 5.31** The variation of η with respect to h/r_0 for ring footing resting on sandy-clayey with ($\phi=40^\circ$) and corresponding to four different radius ratios: (a and e) $r_i/r_0=0$; (b and f) $r_i/r_0=0.25$; (c and g) $r_i/r_0=0.50$; and (d and h) $r_i/r_0=0.75$. 172
- Figure 5.32** The variation of η with respect to h/r_0 for ring footing resting on sandy-clayey with ($\phi = 45^\circ$) and corresponding to four different radius ratios: (a and e) $r_i/r_0=0$; (b and f) $r_i/r_0=0.25$; (c and g) $r_i/r_0=0.50$; and (d and h) $r_i/r_0=0.75$. 173
- Figure 5.33** Failure patterns for ring footing having $r_i/r_0 = 0.25$, rested over (a-c) S-S ($\phi_1=45^\circ$, $\phi_2=30^\circ$); (d-f) C-C ($c_{u1}/(\gamma r_0)=1$, $c_{u2}/(\gamma r_0)=0.5$) and (g-i) S-C ($\phi=40^\circ$, $c_u/(\gamma r_0)=0.5$), soils with loading positions: (a,d,g) L_1 ; (b,e,h) L_2 ; (c,f,i) L_3 . 178
- Figure 5.34** Failure patterns for ring footing having $h/r_0 = 0.25$, rested over (a-c) Type A2 ($\phi_1=40^\circ$, $\phi_2=30^\circ$) and (d-f) Type B2 ($c_{u1}/(\gamma r_0) = 1$, $c_{u2}/(\gamma r_0) = 0.5$) soils, subjected to L_1 loading positions, and corresponding to three different: (a and d) $r_i/r_0=0$; (b and e) $r_i/r_0=0.5$; and (c and f) $r_i/r_0=0.75$ 179

- Figure 5.35** Failure pattern for $\phi=35^\circ$, $c_u/(\gamma r_0)=1$, $h/r_0=2$, and $q/(\gamma r_0)=1$ with: a) $r_i/r_0=0$; b) $r_i/r_0=0.25$; c) $r_i/r_0=0.5$; and d) $r_i/r_0=0.75$. 181
- Figure 5.36** Failure patterns for ring foundation having $\phi_1=40^\circ$, $\phi_2=35^\circ$, $r_i/r_0=0.25$, and $q/(\gamma r_0)=0$, subjected to L_2 loading position, and corresponding to: a) $h/r_0=0.5$; b) $h/r_0=1$; c) $h/r_0=2$; and d) $h/r_0=5$. 182
- Figure 5.37** Failure patterns for ring foundation having $\phi=40^\circ$, $c_u/(\gamma r_0)=0.5$, $r_i/r_0=0.50$, and $q/(\gamma r_0)=0$, subjected to L_2 loading position, and corresponding to: a) $h/r_0=0.5$; b) $h/r_0=2$; and d) $h/r_0=4$. 184
- Figure 5.38** Failure patterns for ring foundation having $c_u/(\gamma r_0)=1$, $h/r_0=2$, and $r_i/r_0=0.25$, subjected to L_2 loading position, and corresponding to: a) $\phi=35^\circ$; b) $\phi=40^\circ$; and c) $\phi=45^\circ$. 184
- Figure 5.39** Failure patterns for ring foundation having $\phi=35^\circ$, $h/r_0=1$, and $r_i/r_0=0.25$, subjected to L_2 loading position, and corresponding to: a) $c_u/(\gamma r_0)=0.1$; b) $c_u/(\gamma r_0)=1$; c) $c_u/(\gamma r_0)=5$; and d) $c_u/(\gamma r_0)=10$. 185
- Figure 6.1** a) Different configurations of loadings applied on the rough ring footing rested over homogenous rocks, as represented in b) three-dimensional form, and c) two-dimensional axisymmetric form. 196
- Figure 6.2** Mesh used for the ring footing for four different radius ratios: a) $r_i/r_0=0$; b) $r_i/r_0=0.25$; c) $r_i/r_0=0.50$ and d) $r_i/r_0=0.75$. 198
- Figure 6.3** (a-b) Representation of the 3-D GHB criterion with different GSI and m_i – (a) $m_i=35$ and varying GSI ; (b) $GSI=100$ and varying m_i ; (c-d) removal of discontinuities on the 3-D GHB yield surface: (c) smoothing edge discontinuities in the octahedral plane; and (d) rounding-off tip discontinuity in the meridian plane. 202
- Figure 6.4** The variation of $N_{\sigma 0}$ with respect to r_i/r_0 and m_i corresponding to $q=0$ and three different loading positions: (a-d) L_1 ; (e-h) L_2 ; and (i-l) L_3 and four different values of GSI : (a,e,i) $GSI=20$; (b,f,j) $GSI=40$; (c,g,k) $GSI=60$; and (d,h,l) $GSI=80$. 207
- Figure 6.5** The variation of $N_{\sigma 0}$ with respect to r_i/r_0 and m_i corresponding to $q=0.5\sigma_{ci}$ and three different loading positions: (a-d) L_1 ; (e-h) L_2 ; and (i-l) L_3 and four different values of GSI : (a,e,i) $GSI=20$; (b,f,j) $GSI=40$; (c,g,k) $GSI=60$; and (d,h,l) $GSI=80$. 208
- Figure 6.6** The variation of $N_{\sigma 0}$ with respect to m_i for different values of GSI and corresponding to (i) various loading positions: (a-d) L_1 ; (e-h) L_3 ; (ii) different ring geometries: (a,b,e,f) $r_i/r_0=0.25$; and (c,d,g,h) 211

$r_i/r_0=0.75$; and (iii) contrasting surcharges: (a,c,e,g) $q/\sigma_{ci} = 0.0$; and (b,d,f,h) $q/\sigma_{ci} = 0.5$.

- Figure 6.7** The variation of $N_{\sigma 0}$ with respect to GSI for different values of r_i/r_0 and corresponding to (i) various loading positions: (a-d) L_1 ; (e-h) L_3 ; (ii) different m_i : (a,b,e,f) $m_i=5$; and (c,d,g,h) $m_i=35$; and (iii) contrasting surcharges: (a,c,e,g) $q/\sigma_{ci} = 0.0$; and (b,d,f,h) $q/\sigma_{ci} = 0.5$. 212
- Figure 6.8** Failure patterns developed in the homogenous rocks with $GSI=90$; $m_i=20$; and $\sigma_{ci}=500$ for different ring footings of radius ratio: (a,d,g) $r_i/r_0=0.0$; (b,e,h) $r_i/r_0=0.25$; (c,f,i) $r_i/r_0=0.50$; and subjected to various loading configurations: (a-c) L_1 ; (d-f) L_2 ; and (g-i) L_3 . 215
- Figure 6.9** Failure patterns developed in the homogenous rocks with varying material properties: (a,d) $GSI=40$; $m_i=10$; (b,e) $GSI=90$; $m_i=10$; and (c,f) $GSI=90$; $m_i=35$; and supporting rings of critical radius ratio subjected to two different loading positions: (a-c) L_1 ; and (d-f) L_3 . 216
- Figure 6.10** Failure patterns developed for ring footing ($r_i/r_0=0.25$) rested over homogenous rocks having $m_i=15$; $GSI=80$; $\sigma_{ci}=500$ with different surcharge pressures: (a,c) $q=0.0$; (b,d) $q=0.5\sigma_{ci}$; and different loading conditions, namely, (a-b) L_1 ; and (c-d) L_3 . 217
- Figure 7.1** The variation of normalized water content with matric suction for different value of: a) α ($=0.01, 0.10, 0.40, 0.80$); b) n ($=2, 4, 6, 8$); c) m ($=0.1, 0.5, 0.8, 1$). 227
- Figure 7.2** The variation of k , for clayey soils ($k_s = 1 \times 10^{-8}$ m/s) having $\alpha = 0.001$ and $\alpha = 0.003$, and sandy soils ($k_s = 1 \times 10^{-5}$ m/s) having $\alpha = 0.1$ and $\alpha = 0.3$. 228
- Figure 7.3** The variation of σ^s with depth above water table for different value of α ($=0.1, 0.3, 0.9$) that corresponded to: (a) $n=2$ and $K_M=0$; (b) $n=4$ and $K_M=0$; (c) $n=8$ and $K_M=0$; (d) $n=2$ and $K_M=2$; and (e) $n=2$ and $K_M=4$. 230
- Figure 7.4** A typical triangular element for performing an upper bound limit analysis. 231
- Figure 7.5** a) Modified MC yield surface and its linearization; and b) modified MC yield envelope. 232

Figure 7.6	a) Nodal velocity variables along the velocity discontinuity; and b) nodal velocities and prescribed velocities on a boundary node, <i>i</i> .	235
Figure 7.7	a) Strip footing rested over unsaturated sandy layer; b) Chosen domain with mesh.	244
Figure 7.8	The variation in $N_{\gamma s}$ and $N_{q s}$ for sandy soil with $\phi=30^\circ$ and $K_M=0$ and that correspond to five α 's and four different values of: a) $n=$ 2; b) $n=4$; c) $n=5$; and d) $n=8$.	246
Figure 7.9	The variation in $N_{\gamma s}$ and $N_{q s}$ for sandy soil that had different combinations of α and n that correspond to $K_M=0$ and for four different values of: (a–d) $\phi=35^\circ$; (e–h) $\phi=40^\circ$; and (i–l) $\phi=45^\circ$.	248
Figure 7.10	The variation in $N_{\gamma s}$ and $N_{q s}$ for sandy soil that had different combinations of α and n that correspond to $K_M=2$ and for four different values of: (a–d) $\phi=35^\circ$; (e–h) $\phi=40^\circ$; and (i–l) $\phi=45^\circ$.	249
Figure 7.11	The variation in $N_{\gamma s}$ and $N_{q s}$ for sandy soil that had different combinations of α and n that correspond to $K_M=4$ and for four different values of: (a–d) $\phi=35^\circ$; (e–h) $\phi=40^\circ$; and (i–l) $\phi=45^\circ$.	250
Figure 7.12	The variation in $N_{\gamma s}$ and $N_{q s}$ for sandy soil ($\phi=35^\circ, 45^\circ$) with respect to α for different value of h_w that corresponds to $K_M=0$ and four different values of: a) $\phi=35^\circ, n=2$; b) $\phi=35^\circ, n=4$; c) $\phi=35^\circ, n=5$; d) $\phi=35^\circ, n=8$; e) $\phi=45^\circ, n=2$; f) $\phi=45^\circ, n=4$; g) $\phi=45^\circ, n=5$; h) $\phi=45^\circ, n=8$.	253
Figure 7.13	Nodal velocity patterns for strip footing that rested on unsaturated sands with $\phi=35^\circ$ for varying water table positions ($h_w/b=0, 2,$ and 4) that correspond to: (a–c) ponderable surcharge-less soil; and (d–f) weightless soil with surcharge.	255
Figure 7.14	Nodal velocity pattern for strip footing on sandy soil ($\phi=40^\circ$) for different n values: a) $n=2$; b) $n=4$; c) $n=8$.	256
Figure 7.15	Nodal velocity pattern for strip footing on sandy soil ($\phi=40^\circ$) for different α values: a) $\alpha=0.1$; b) $\alpha=0.5$; c) $\alpha=0.9$.	258
Figure 7.16	Nodal velocity pattern for strip footing on sandy soil ($\phi=40^\circ$) for different K_M values: a) $K_M=0$; b) $K_M=2$; c) $K_M=4$	258
Figure 8.1	a) Domain used for strip footing resting on sandy soil; and b) mesh used for analysis.	265

Figure 8.2	Rigid footing subjected to inclined and eccentric load	267
Figure 8.3	The variation of UBC (p_u) with respect to GWT for sands with $\phi' = 35^\circ$, $e/B = 0$, and subjected to three β : (a-d) $\beta=0^\circ$; (e-h) $\beta=10^\circ$; and (i-l) $\beta=20^\circ$; and corresponding to four values of n : (a,e,i) $n = 2$; (b,f,j) $n = 3$; (c,g,k) $n = 4$; and (d,h,l) $n = 5$.	270
Figure 8.4	The variation of UBC (p_u) with respect to GWT for sands with $\phi' = 35^\circ$, $e/B = 0.25$, and subjected to three β : (a-d) $\beta=0^\circ$; (e-h) $\beta=10^\circ$; and (i-l) $\beta=20^\circ$; and corresponding to four values of n : (a,e,i) $n = 2$; (b,f,j) $n = 3$; (c,g,k) $n = 4$; and (d,h,l) $n = 5$.	271
Figure 8.5	The variation of UBC (p_u) with respect to GWT for sands with $\phi' = 35^\circ$, $e/B = - 0.25$, and subjected to two β : (a,c,e,g) $\beta=10^\circ$; (b, d, f, h) $\beta=20^\circ$; and corresponding to four values of n : (a,b) $n = 2$; (c,d) $n = 3$; (e,f) $n = 4$; and (g,h) $n = 5$.	272
Figure 8.6	The variation of UBC (p_u) with respect to GWT for sands with $\phi' = 45^\circ$, $e/B = 0$, and subjected to three β : (a-d) $\beta=0^\circ$; (e-h) $\beta=10^\circ$; and (i-l) $\beta=20^\circ$; and corresponding to four values of n : (a,e,i) $n = 2$; (b,f,j) $n = 3$; (c,g,k) $n = 4$; and (d,h,l) $n = 5$.	273
Figure 8.7	The variation of UBC (p_u) with respect to GWT for sands with $\phi' = 45^\circ$, $e/B = 0.25$, and subjected to three β : (a-d) $\beta=0^\circ$; (e-h) $\beta=10^\circ$; and (i-l) $\beta=20^\circ$; and corresponding to four values of n : (a,e,i) $n = 2$, (b,f,j) $n = 3$, (c,g,k) $n = 4$, and (d,h,l) $n = 5$.	274
Figure 8.8	The variation of UBC (p_u) with respect to GWT for sands with $\phi' = 45^\circ$, $e/B = - 0.25$ and subjected to two β : (a,c,e,g) $\beta=10^\circ$; (b, d, f, h) $\beta=20^\circ$; and corresponding to four values of n : (a,b) $n = 2$; (c,d) $n = 3$; (e,f) $n = 4$; and (g,h) $n = 5$.	275
Figure 8.9	The variation of p_u with respect to GWT for sands with $\phi' = 45^\circ$ and corresponding to: (a) $n = 1.2$, $e/B=0.25$; (b) $n = 1.5$, $e/B=0.25$; (c) $n = 1.2$, $e/B=0$; (d) $n = 1.5$, $e/B=0$; (e) $n = 1.2$, $e/B=-0.25$; and (f) $n = 1.5$, $e/B= - 0.25$.	277
Figure 8.10	Interaction diagram in the $V/V_{max} - H/V_{max}$ plane for $\phi' = 35^\circ$, $\alpha = 0.1 \text{ kPa}^{-1}$ and different value of h_w and n .	281
Figure 8.11	Interaction diagram in the $V/V_{max} - H/V_{max}$ plane for $\phi' = 30^\circ$, $n = 4$ and different value of h_w and a .	
Figure 8.12	Nodal velocity pattern for strip footing on sandy soil ($\phi' = 35^\circ$) for different e and β values: a) $e/B = 0$, $\beta=0^\circ$; b) $e/B = 0$, $\beta=10^\circ$; c) $e/B = 0$, $\beta=20^\circ$; d) $e/B = 0.25$, $\beta=0^\circ$; e) $e/B = 0.25$, $\beta=10^\circ$; f) $e/B =$	283

0.25, $\beta=20^\circ$.

- Figure 8.13** Nodal velocity pattern for strip footing subjected to vertical and eccentric loading and the supporting unsaturated sand having $\phi' = 45^\circ$ and different α : a) $\alpha = 0.1$; b) $\alpha = 0.3$; c) $\alpha = 0.5$. 285
- Figure 8.14** Nodal velocity pattern for strip footing subjected to vertical and eccentric loading and the supporting unsaturated sand having $\phi' = 45^\circ$ with two n values: a) $n = 2$; and b) $n = 4$. 288
- Figure 8.15** Nodal velocity pattern for strip footing subjected to vertical and eccentric loading and the supporting sand having different ϕ' : a) $\phi' = 35^\circ$; b) $\phi' = 45^\circ$. 289
- Figure 8.16** The nodal velocity pattern for strip footing subjected to vertical and concentric loading and the supporting sands ($\phi' = 45^\circ$) having different GWT position: a) $h_w/B = 3$; b) $h_w/B = 2$; c) $h_w/B = 1$. 290
- Figure 9.1** a) Domain used for strip footing resting on sandy soil; and b) mesh used for analysis. 294
- Figure 9.2** The profiles of the normalized (a,c) matric suction and (b,d) suction stress for an unsaturated sand layer under transient infiltration with α equals: (a-b) 0.7; and (c-d) 0.9. 300
- Figure 9.3** A comparative study of the present numerical solutions with the analytical solutions of Shahrokhbadi *et al.* (2019) in terms of: (a) ψ_{norm} ; and (b) σ_{norm}^s curves. 301
- Figure 9.4** The temporal variation of $p_w/(\gamma B)$ for strip footing resting on unsaturated sand ($\phi=30^\circ$) with: a) $h_w/b=1$; b) $h_w/b=2$; c) $h_w/b=3$; d) $h_w/b=4$. 304
- Figure 9.5** The temporal variation of $p_w/(\gamma B)$ for strip footing resting on unsaturated sand ($\phi=35^\circ$) with: a) $h_w/b=1$; b) $h_w/b=2$; c) $h_w/b=3$; d) $h_w/b=4$. 304
- Figure 9.6** The temporal variation of $p_w/(\gamma B)$ for strip footing resting on unsaturated sand ($\phi=40^\circ$) with: a) $h_w/b=1$; b) $h_w/b=2$; c) $h_w/b=3$; d) $h_w/b=4$. 305
- Figure 9.7** The temporal variation of $p_w/(\gamma B)$ for strip footing resting on unsaturated sand ($\phi = 40^\circ$) with: a) $h_w/b=1$; b) $h_w/b=2$; c) $h_w/b=3$; 305

d) $h_w/b=4$.

- Figure 9.8** The variation of normalized bearing capacity ($p_u/\gamma B$) of strip footing with respect to the friction angle (ϕ) for: a) $t = 1$ day; b) $t = 4$ days. 307
- Figure 9.9** The temporal variation of normalized bearing capacity ($p_u/\gamma B$) of strip footing resting on unsaturated sand ($\phi = 35^\circ$) with: (a) $\alpha = 0.6$, $\theta_r = 0.41$, $\theta_s = 0.05$; (b) $\alpha = 0.8$, $\theta_r = 0.41$, $\theta_s = 0.05$. 307
- Figure 9.10** The nodal velocity pattern for strip footing on unsaturated sands with $\phi = 45^\circ$ corresponding to: a) $t = 1$ day; b) $t = 4$ days c) $t = 8$ days. 309
- Figure 9.11** The nodal velocity pattern for strip footing on s unsaturated sands with $\phi = 40^\circ$ corresponding to: a) $\alpha = 0.6$; b) $\alpha = 0.7$ c) $\alpha = 0.9$. 309
- Figure 9.12** The nodal velocity pattern for strip footing on unsaturated sand with $\phi = 35^\circ$ and $t = 1$ day corresponding to: a) $q/k_s = 0.1$; b) $q/k_s = 0.5$; c) $q/k_s = 1$. 311
- Figure 9.13** The nodal velocity pattern for strip footing on unsaturated sand with $\phi = 35^\circ$ and $t = 1$ day corresponding to: a) $h_w/b = 1$; b) $h_w/b = 2$; c) $h_w/b = 3$. 311

LIST OF NOTATIONS

- a = Square of the radius of the Mohr circle of any point for the current stress state
- a_{11}^e = Local matrix defined in Equation (7.17)
- a_{12}^e = Local matrix defined in Equation (7.17)
- a_{21} = Local matrix defined in Equation (7.25)
- a_{23} = Local matrix defined in Equation (7.25)
- a_{31} = Local matrix defined in Equation (7.27)
- a_{eq}^e = Local coefficient matrix of element equilibrium defined in Equation (3.5)
- a_{eq}^{dc} = Local coefficient matrix of discontinuity equilibrium defined in Equation (3.8)
- a_{eq}^{bd} = Local coefficient matrix of stress boundary condition defined in Equation (3.10)
- A_{11} = Global matrix defined in Equation (7.43a)
- A_{12} = Global matrix defined in Equation (7.43a)
- A_{21} = Global matrix defined in Equation (7.43a)
- A_{23} = Global matrix defined in Equation (7.43c)
- A_{31} = Global matrix defined in Equation (7.43c)
- A^e = Area of triangular element
- A_{eq} = Global matrix defined in Equation (3.32a)
- b_{eq}^e = Vector associated with element equilibrium defined in Equation (3.5)
- b_{eq}^{dc} = Vector associated with element equilibrium defined in Equation (3.8)
- b_{eq}^{bd} = Vector associated with stress boundary condition defined in Equation (3.10)
- b = Half width of the strip footing
- B = Width of strip footing /diameter of the circular pile
- B_{eq} = Global vector defined in Equation(3.23b)

c'	=	Effective cohesion
c	=	Cohesion of soil
c_o	=	Cohesion of soil at the ground surface
c_b	=	Cohesion at the level of pile base
c_u	=	Undrained shear strength of the clayey strata
C_1	=	Global vector defined in Equation (7.43a)
C_2	=	Global vector defined in Equation (7.43a)
C_3	=	Global vector defined in Equation (7.43a)
d	=	Square of the radius of the Mohr circle at failure as defined in Equation (3.5)
d_x	=	Search direction vector as defined in Equation (3.30)
D	=	Vertical extent of domain below the pile
D_c	=	Total number of stress/velocity discontinuities
D_f	=	Disturbance factor
D_i	=	Inner diameter of ring footing
D_o	=	Outer diameter of ring footing
e	=	Load eccentricity
E	=	Total number of elements in the domain
F_1	=	Form of the modified MC* yield circle
F_2	=	Form of the modified MC yield envelope
GSI	=	Geological Strength Index
$g(\sigma)$	=	Set of inequality constraints defined in Equation (3.23c)
h	=	Thickness of upper soil
h_{opt}	=	Optimum thickness of the upper layer
h_w	=	Water table depth
h_{wcr}	=	Critical water table depth
H	=	Length of the circular pile (Chapter3)/ Vertical extent of domain
I	=	Unit matrix
k_s	=	Saturated hydraulic conductivity
K_r	=	Relative hydraulic conductivity

* MC=Mohr-Coulomb

K_M	=	Mualem's variable relating the vG-SWRC model parameters m and n
h_m	=	Matric suction head
l	=	Side length of an element
L_g	=	Horizontal extent of the domain measured
L_s	=	Length of boundary edge between two boundary nodes
L_0	=	Complete loading condition
L_1	=	Inner half loading condition
L_2	=	Middle half loading condition
L_3	=	Outer half loading condition
m	=	Rate at which the cohesion increases linearly with depth (Chapter 3)/ nondimensional strength parameter of OHB* criterion (Chapter 6)/ vG parameter (Chapter 7)
m_b	=	Broken rock mass strength parameter of GHB** criterion as defined in Equation (6.1b)
m_i	=	Value of m for intact rock mass
n	=	Total number of unknown stress variables (Chapter 3)/ Pore size spectrum number (Chapter 7)
N_b	=	Number of nodes where the boundary stress/velocities are prescribed
N	=	Number of nodes
N_c	=	Bearing capacity factor due to cohesion
N_i	=	Shape function of i^{th} node of triangular element
N_{qs}	=	Bearing capacity factor due to surcharge pressure for unsaturated soil
N_s	=	Total number of nodes along the footing–soil interface
N_γ	=	Bearing capacity factor due to unit weight of soil
N_q	=	Bearing capacity factor due to surcharge
$N_{\gamma s}$	=	Bearing capacity factor due to unit weight for unsaturated soil
N_σ	=	Non-dimensional bearing capacity factor for rock mass
$N_{\sigma 0}$	=	Nondimensional bearing capacity factor for the weightless rock mass
* OHB= Ordinary Hoek-Brown		
* GHB= Generalized Hoek-Brown		

p	=	Number of sides of a polygon required to linearize the MC yield criterion
p_u	=	Ultimate bearing capacity of footing
P_{1e}	=	Rate of work done by the body forces
P_{2e}	=	Power dissipation in an element due to plastic deformation
P_{3d}	=	Power dissipation along a velocity discontinuity
P_{ext}	=	Rate of the external work done defined in Equation (7.28)
P_{int}	=	Internal power dissipation defined in Equation (7.29)
q	=	Normal surcharge (Chapter 3)/discharge flow rate (Chapter 7)
q_s	=	Surcharge pressure on unsaturated soil
Q	=	Vertical compressive downward load of magnitude
Q_u	=	Maximum vertical compressive downward load of magnitude
\bar{r}	=	Horizontal distance between the centroid of the triangle element and axis of the footing
r_0	=	Outer radius of ring footing
r_i	=	Inner radius of ring footing
r_s	=	Mean radius of boundary edge L_s
s	=	Slack variable
s	=	Nondimensional strength parameter of OHB criterion
S_r	=	Residual degree of saturation
S_e	=	Effectivel degree of saturation
S	=	Degree of saturation
t_1 and t_2	=	Prescribed shear stresses at boundary edge
t_{cr}	=	critical time
u	=	Horizontal velocity (unknown)
u_a	=	Pore air pressure
u_w	=	Pore water pressure
u_{ij}^+, u_{ij}^-	=	Non-negative velocity discontinuity
v	=	Vertical velocity (unknown)
Δu	=	Normal velocity jump

Δv	=	Tangential velocity jump
v_n	=	Velocity specified for the footing nodes
y	=	Distance above water table
Z_{inf}	=	Zone of influence
$\dot{\lambda}$	=	Non-negative plastic multiplier rate
λ	=	Lagrangian multiplier for the inequality constraints
ν	=	Lagrangian multiplier for the equality constraints
$\dot{\epsilon}_{xx}$	=	Plastic normal strain rates in x direction
$\dot{\epsilon}_{zz}$	=	Plastic normal strain rates in z direction
$\dot{\gamma}_{xz}$	=	Plastic shear strain rates in xz direction
γ	=	Unit density of soil
η	=	Efficiency factor
μ^k	=	Barrier parameter at k^{th} iteration
δ	=	Interface friction angle between footing and adjoining soil mass
Ψ	=	Angle made by the footing-soil interface with $+r$ -axis
$\bar{\sigma}$	=	Stress invariant by permuting $\bar{\sigma}$ with a small term ϵ
$\bar{\sigma}$	=	Octahedral/Deviatoric Stress
σ_n	=	Normal stress acting on a plane
σ_{nt}	=	Shear stress acting along a plane
σ_r	=	Normal stress in r direction
σ_z	=	Normal stress in z direction
σ_m	=	Hydrostatic Stress
σ_{ci}	=	Uniaxial compressive strength of intact rock
σ_1	=	Major principal stress
σ_3	=	Minor principal stress
σ^s	=	Suction stress
σ_θ	=	Hoop stress

σ'	=	effective normal stress
σ_2	=	intermediate principal stress
θ	=	Lode angle (Chapter 3) / circumferential direction(Chapter 3) /volumetric water content (Chapter 7)
θ_r	=	Residual volumetric water content
θ_s	=	Saturated volumetric water content
Θ_n	=	Normalized water content
θ_T	=	Transition angle
τ_{rz}	=	Shear stress in r - z plane
μ^k	=	Barrier parameter
$f(\sigma)$	=	Yield condition
$h(\sigma)$	=	Set of inequality constraints defined in Equation (3.14)
$u(\sigma)$	=	Set of inequality constraints defined in Equation (3.14)
β	=	Inclination of load
χ	=	Saturation-state-dependent single valued effective stress parameter
γ_w	=	Unit weight of water
δ	=	Interface friction angle between the footing base and soil
ϕ	=	Angle of friction of soil
ϕ_u	=	Undrained cohesion
ϕ'	=	Effective angle of friction of soil
ϕ_b	=	Angle indicating the rate of increase in shear strength with respect to a change in matric suction
ψ	=	Dilation angle (Chapter 4)/ matric suction (Chapter 7)
α_b	=	Adhesion factors for pile base cohesion
α_s	=	Adhesion factors for and pile shaft-soil interface cohesion
α	=	Exponential term in the GHB criterion (Chapter 6)/air entry parameter (Chapter 7)
ε	=	Offset distance along hydrostatic axis for smoothing the apex of the yield (MC/GHB) pyramid
η	=	Efficiency factor accounts for the presence of sand layer over clayey stratum

ω = Angle made by the stress with $+r$ -axis /velocity discontinuity line with $+x$ -
axis

Ω = Angle made by the stress with $+r$ -axis /velocity discontinuity line with $+x$ -
axis

LIST OF TABLES

Table No.	Title	Page No.
Table 3.1.	A comparison of present N_c values with those from literature with $\alpha_b = 0$, $\alpha_s = 0$.	85
Table 3.2.	A comparison of present N_c values with those from literature with $\alpha_b = 1$, $\alpha_s = 0$.	86
Table 4.1.	The ultimate bearing capacity of ring footing placed on homogenous clays for different combination of r_i/r_0 , m , and $q/(\gamma r_0)$.	97
Table 4.2.	The variation of h_{opt}/r_0 corresponding to $c_u/(\gamma r_0) = 1$, and for different values of ϕ , m , r_i/r_0 , and $q/(\gamma r_0)$.	107
Table 4.3.	The variation of η corresponding to $q/(\gamma r_0)=0.5$, $m=0$, and for various combinations of ϕ , h/r_0 , $c_u/(\gamma r_0)$, and r_i/r_0 .	108
Table 4.4.	The variation of η corresponding to $c_u/(\gamma r_0)=0.5$, $m=0$, and for various combinations of ϕ , h/r_0 , $q/(\gamma r_0)$, and r_i/r_0 .	110
Table 4.5.	A comparison of N_c for rough circular footing ($r_i/r_0=0$) resting on homogenous clay.	121
Table 4.6.	A comparison of N_γ for rough circular footing ($r_i/r_0=0$) resting on homogenous sands.	122
Table 4.7.	A comparison of $p_u/(\gamma r_0)$ for circular footing ($r_i/r_0=0$, $r_0=1.5m$, and $\phi= 40^\circ$) resting over sand-clay medium with different values of h/r_0 and $c_u/(\gamma r_0)$.	124
Table 4.8.	A comparison of N_γ values for ring footing on sand layer with ϕ equals to 20° , 25° , 30° , 40° , and r_i/r_0 equals to 0.25, 0.5, 0.75.	125
Table 4.9.	Comparison of N_γ values for ring footing on homogenous sand	126
Table 5.1.	The ultimate bearing capacity (p_u) of ring footing placed on homogenous sands and clays for different combination of r_i/r_0 , $q/(\gamma r_0)$ and loading positions.	136
Table 5.2.	The variation of efficiency factor (η) for ring footing resting on layered sands ($\phi_1=35^\circ$ and $\phi_2=40^\circ$) and corresponding to various loading positions, ri/r_0 and h/r_0 .	146
Table 5.3.	The variation of h_{opt}/r_0 corresponding to different values of ϕ_1 , ϕ_2 , r_i/r_0 , and $q/(\gamma r_0)$.	152

Table 5.4.	The variation of h_{opt}/r_0 corresponding to different values of $c_{u1}/(\gamma r_0)$, $c_{u2}/(\gamma r_0)$, r_i/r_0 , and $q/(\gamma r_0)$.	160
Table 5.5.	The variation of h_{opt}/r_0 corresponding to different values of ϕ , $c_u/(\gamma r_0)$, r_i/r_0 , and $q/(\gamma r_0)$.	176
Table 5.6.	A comparison of N_c values for ring footing on clay–clay layer for L_0 loading.	187
Table 5.7.	A comparison of N_γ values for ring footing on sand–sand layered soil for L_0 loading.	187
Table 5.8.	A comparison of N_c and N_γ for ring footing resting on homogenous soils for different loading positions.	189
Table 6.1.	A comparison of N_{σ_0} for different loading positions on various rings rested over rocks of different strengths	205
Table 6.2.	A comparison of N_σ values for circular footing ($r_i/r_0 = 0$) using different methods.	219
Table 6.3.	A comparison of N_{σ_0} values for ring footing on rock mass.	221
Table 7.1.	The variation of N_γ for $K_M = 0$ and different values of n , α , ϕ , and δ/ϕ .	251
Table 7.2	A comparison of q_u values for strip footing resting on unsaturated sandy soil.	259
Table 8.1.	A comparative study of UBC to check the effect of three combinations of concentric/eccentric and vertical/inclined loading on strip foundation rested over unsaturated sands ($\phi = 35^\circ$) with various α and n values and fluctuating GWT.	279
Table 8.2.	The variation of q_u for positive and negative eccentricity corresponding to various hydromechanical properties of soil.	280
Table 8.3.	A Comparison of reduction factor (RF) values for strip footing resting on sandy soil subjected to combined loading.	291